

Near static strain measurement with piezoelectric films

Arun K. Ramanathan, Leon M. Headings, Marcelo J. Dapino *

NSF IUCRC on Smart Vehicle Concepts, Department of Mechanical and Aerospace Engineering, The Ohio State University, USA



ARTICLE INFO

Article history:

Received 1 August 2019

Received in revised form

16 September 2019

Accepted 2 October 2019

Available online 17 November 2019

Keywords:

Flexible piezoelectric sensors

PVDF

Strain measurement

Compensated charge amplifier

Static sensing

ABSTRACT

A fundamental challenge that prevents the implementation of piezoelectric sensors for measuring extremely low frequency (<1 mHz) events, such as aerodynamic pressure measurements, earthquake detection, and physiological monitoring, is their inability to measure static or very low frequency signals. To enable near static measurements, we present a low-noise, differential charge amplifier topology that performs real-time cancellation of drift in the output voltage while simultaneously increasing the gain of a conventional charge amplifier. A sensing frequency range from 0.01 mHz to 310 kHz with a voltage drift reduction of up to 95% is demonstrated. A theoretical sensitivity increase of up to 30 dB is achieved with the proposed topology compared to a basic charge amplifier with the same component tolerances, time constant, and allowable drift rate. The proposed circuit is interfaced with a piezoelectric PVDF film for evaluation of performance in the time and frequency domains. The measured voltage from uniaxial near DC strain measurements stays within 3% over a measurement period of 500 s. The paper further describes a linear piezoelectric strain sensor model and the various factors that influences the charge output, loading effect, and lateral cross-sensitivity of the sensor. The calculated strain–voltage relationship or the gage sensitivity agrees well with the measurements with a linearity error of less than 5% up to 1 millistrain.

© 2019 Elsevier B.V. All rights reserved.

1. Introduction

There is a need for non-intrusive, low profile, and high-performance strain sensors in a range of applications from human motion monitoring [1] to high end torque measurements [2]. Dimensional changes and structural deformations form the sensing mechanism of resistive and capacitive strain gages. The gage factor of a resistive or capacitive sensor is respectively proportional to the ratio of resistance or capacitance change over measured strain. Commercial metal-foil based strain sensors possess gage factors in the range of 1–3, whereas semiconductor-based piezoresistive sensors achieve gage factors greater than 100 [3]. Piezoresistive sensors use a full Wheatstone bridge to convert resistance change to output voltage. Strain resolution is defined as the smallest strain a sensor can reliably indicate above the peak-to-peak range of the noise in the output voltage. For a given gage factor, the voltage sensitivity of a piezoresistive sensor is proportional to the bridge excitation voltage V_E [4]. However, increasing V_E also amplifies the transducer noise, thus limiting the resolution of the sensor unless other design constraints, such as size, power consumption,

and complexity of the conditioning electronics, are relaxed. Capacitive strain sensors are advantageous considering their low power requirement, low electrical noise, and cost-effectiveness. However, they exhibit low sensitivity and a slower response time when subjected to large strains compared to piezoresistive sensors [5].

Polyvinylidene fluoride (PVDF) is a flexible polymer that exhibits strong piezoelectricity in its β -phase. It can be manufactured as a thin sheet and is conformable to arbitrarily shaped structures. Its elastic modulus is approximately a thirtieth of piezoceramics such as PZT, thus making it non-intrusive for large strain or high frequency measurements [6]. Despite its relatively low piezoelectric charge coefficient, it is suitable for high frequency applications due to its low density. Table 1 compares the relevant parameters of current strain sensing technologies. One of the fundamental drawbacks of piezoelectric sensors is their inability to hold the charge displaced by a stress applied to it. Thus, they are intrinsically unsuitable for the measurement of static or low frequency strain inputs. For this reason, they are mostly used in strain rate measurements [8,9].

Several techniques have been proposed to improve the static measurement ability of piezoelectric sensors. These techniques can be broadly classified into two types: resonator type and charge readout type. The resonator type static force measurement technique involves a piezoelectric structure actuated near its resonance frequency. Any applied stress causes a shift in the resonant

* Corresponding author at: Department of Mechanical and Aerospace Engineering, The Ohio State University, 201 W. 19th Avenue, Columbus, OH 43210, USA.

E-mail address: dapino.1@osu.edu (M.J. Dapino).

Table 1

Comparison of strain sensing technologies.

Technology	Type	Sensing material	Gage factor (25 °C)	Sensitivity, $V_E = 10 \text{ V} (\text{mV } \mu\text{e}^{-1})$	Resolution (μe)	Lowest possible measurement frequency (Hz)
Piezoresistive [3]	Metal	Constantan	1–3	0.01–0.03	20	DC
	Semiconductor	Silicon	100–175	1–1.75	0.4	DC
Capacitive [5]	Elastomer	SEBS	2	–	25	DC
Piezoelectric [7]	Piezoceramic	PZT	–	50	$\approx 10^{-4}$	20
Piezoelectric (this work)	Flexible polymer	PVDF	–	0.29	0.25	10^{-5}

frequency [10] or changes the electrical admittance at a fixed frequency [11]. Therefore, the changes in dynamic characteristics are related to the strain in the sensor. However, the low sensitivity and the complexity of the associated signal conditioning electronics diminish the advantages of this approach over conventional piezoresistive strain gages.

The charge readout type involves direct integration of the charge output from a piezoelectric sensor using a large time constant charge amplifier. Due to the compactness and flexibility of this technique, it has greatly increased the number of low frequency applications of piezoelectric sensors, such as pressure sensing [12], prestress measurements [13], physiological measurements [14], and characterization of the piezoelectric materials themselves [15,16]. The limitation of a large time constant charge amplifier is a drifting output voltage due to the input bias current of the operational amplifier that restricts its operational time and direct readout capability. Park et al. [17] developed one of the earliest charge readout algorithms to circumvent this issue. The technique uses periodic resetting of the feedback capacitor and digital integration of the output signal from the charge amplifier. This implementation is similar to the commercially available IVC102 transimpedance chip demonstrated in long time static load measurements [18]. However, the integrated signal accumulates error due to charge injection during periodic switching. Brandolini et al. [19] demonstrated a balanced configuration of the charge amplifier to overcome this disadvantage, but the proposed circuit performs digital integration of the measured voltage signal, thus placing a hard limit on the upper cutoff frequency of the system. Gavin et al. [20] developed a hybrid digital-analog integrator to eliminate drift in the output voltage. Though the technique improved the quasi-static performance of the system, the conventional charge amplifier performs better in transient operations. A single-ended drift compensation technique was demonstrated using a compensated charge amplifier for near static force measurements [21]. Its drawback is that unwanted current signals such as DC offset or input bias currents appear as common-mode current.

A differential-input, differential-output configuration offers a clear advantage over a single-ended configuration for better signal-to-noise ratio [22]. However, the design of a discretely implemented large time constant differential charge amplifier with a characterization of its effect on sensor calibration for long time static and low frequency (under 20 Hz) dynamic measurements is not available in the literature. The potential applications that could benefit from these measurement capabilities include surface pressure measurements in automotive wind tunnel experiments, earthquake detection, physiological monitoring, and characterization of the relaxation response of highly compliant structures. The objective of this article is to demonstrate a straightforward differential compensated charge amplifier using discrete components for near static and low frequency strain measurements with piezoelectric strain sensors. The proposed configuration provides real-time drift cancellation through parallel charge amplifiers with equal charge sensitivity, enabling a direct readout of the state of strain in the sensor. The signal processor is simple, small, and typically consumes power on the order of a few milliwatts. Hence, it is attractive for applications where the sensor and the associated electronics

can only be powered using low power batteries or energy harvesters. The differential configuration of the charge-amplification stage with only capacitors further improves the signal-to-noise ratio of the sensor relative to a basic charge amplifier.

A generalized piezoelectric strain sensor model is presented in Section 2. A single-ended basic charge amplifier model is developed and the effects of sensor and feedback impedances on the sensitivity, time constant, and voltage drift rate are presented in Section 3. A compensated charge amplifier topology and the effect of component tolerances on the sensitivity and residual voltage drift rate are discussed in Section 4. Characterization experiments aimed at evaluating the performance of the uniaxial PVDF strain sensor interfaced with the proposed circuit topology are presented in Section 5. The experiments are further utilized to validate the developed strain sensor model under static and low frequency strain inputs.

2. Piezoelectric strain sensors

Piezoelectric transducers produce strain in response to an applied electric field or generate charge displacement as a result of applied mechanical stress. Fig. 1 shows the usual coordinate axes of a piezoelectric sensor. Based on the planar nature of the piezoelectric laminae, it can be assumed that any line perpendicular to the neutral plane of the host structure before deformation remains perpendicular after deformation. Thus, a plane stress approximation can be used to model the stress induced on the sensor [23]. Due to the lower thickness and elastic moduli of the piezoelectric strain sensor in comparison with the host structure, the effect of shear lag due to the thickness of the adhesive layer is negligible [6]. Assuming isothermal conditions with no externally applied electric field and also neglecting the effect of electric field due to the generated charge displacement, the decoupled linear piezoelectric equations are given by

$$D_3 = d_{31}T_1 + d_{32}T_2 \quad (1)$$

$$\begin{Bmatrix} T_1 \\ T_2 \end{Bmatrix} = \frac{Y_1}{1 - \nu_1\nu_2} \begin{bmatrix} 1 & \nu_1 \\ \nu_2 & \frac{Y_2}{Y_1} \end{bmatrix} \begin{Bmatrix} \varepsilon_1 \\ \varepsilon_2 \end{Bmatrix}, \quad (2)$$

where D_3 , ε_1 , and ε_2 are the electric displacement and in-plane strains along the directions specified by the subscripts, respectively; T_1 and T_2 are the in-plane stresses in the piezoelectric sensor; Y_1 and Y_2 are the in-plane elastic moduli; ν_1 and ν_2 are the Poisson's ratios along the in-plane directions. The piezoelectric charge coefficients are given by d_{31} and d_{32} .

The electric displacement in terms of the in-plane strains is obtained using (2) in (1) as

$$D_3 = \frac{1}{1 - \nu_1\nu_2} [(d_{31} + \nu_2 d_{32})Y_1 \varepsilon_1 + (d_{32} + \nu_1 d_{31})Y_2 \varepsilon_2]. \quad (3)$$

Integration over electrode area A_S gives the net charge produced by the sensor,

$$Q = \frac{1}{1 - \nu_1\nu_2} \left[(d_{31} + \nu_2 d_{32})Y_1 \oint \varepsilon_1 dA_S + (d_{32} + \nu_1 d_{31})Y_2 \oint \varepsilon_2 dA_S \right]. \quad (4)$$

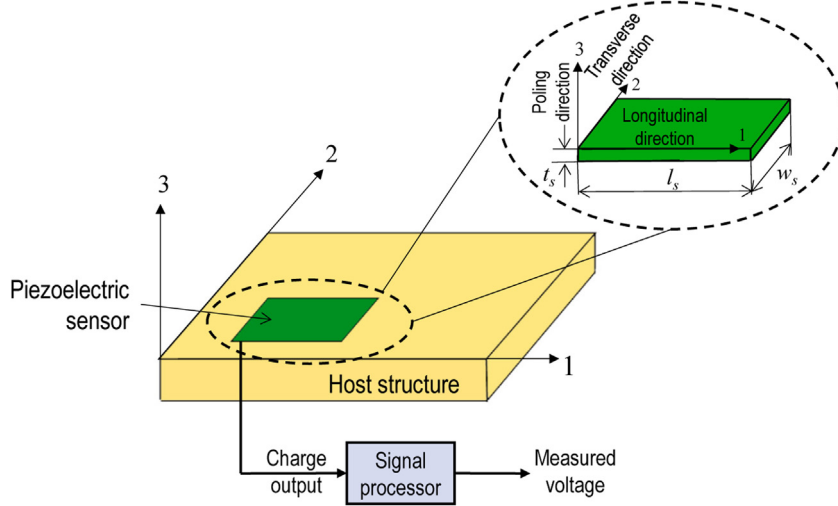


Fig. 1. Schematic of a piezoelectric strain sensor attached to a host structure.

Table 2

Comparison of elastic moduli, charge coefficients, and lateral sensitivity coefficients of different piezoelectric materials.

Parameter	PVDF [25]	PZT-5H [6,26]	MFC [27]
\$Y_1\$ (GPa)	2–4	71	30
\$d_{31}\$ (pCN\$^{-1}\$)	21	−274	−170
\$v_1\$	0.35	0.31	0.31
\$a_r\$	0.6	1	0.52
\$d_r\$	0.22	1	0.59
\$\kappa\$	0.33	1	0.43

Note that the piezoelectric strain sensor generates charge proportional to the average in-plane strains on the sensor. As a result, if there are large strain variations along the surface area of the sensor, the calculated strain due to the charge output would not represent the maximum strain. Also, in the case of stress propagation, the charge output from the sensor will not only depend on the amplitude of the stress wave but also on its frequency [24]. Thus, the position, shape, and dimensions of the sensor have to be chosen such that the variation along the gage area of the sensor is minimal. The distributed measurement over large surfaces with piezoelectric sensors is an advantage over resistive gages in shape estimation algorithms [5]. Letting

$$a_r = \frac{Y_2}{Y_1} = \frac{\nu_2}{\nu_1} \text{ and } d_r = \frac{d_{32}}{d_{31}},$$

(4) can be rewritten as

$$Q = \frac{Y_1 d_{31}}{1 - a_r \nu_1^2} \left[(1 + a_r d_r \nu_1) \oint \varepsilon_1 dA_S + a_r (d_r + \nu_1) \oint \varepsilon_2 dA_S \right]. \quad (5)$$

The process of stretching the film during manufacturing orients the polymer chains in a specific direction and renders the material elastically anisotropic and piezoelectrically orthotropic. For some piezoelectric films that are drawn four times their original length, the Poisson's ratios exceed the upper limit of an isotropic material, i.e., \$\nu > 0.5\$ [23]. Let \$\kappa\$ be the lateral sensitivity coefficient of the sensor defined as

$$\kappa = \frac{a_r(d_r + \nu_1)}{(1 + a_r d_r \nu_1)}. \quad (6)$$

For typical piezoelectric materials, \$a_r\$ varies from 0.5 to 1 and \$d_r\$ varies from 0.1 to 1. Table 2 shows the properties of different piezoelectric materials. It is noted that the assumptions of non-directionality, i.e., \$a_r=1\$, and no lateral cross-sensitivity, i.e., \$d_r=1\$, would lead to significant error in uniaxial strain measure-

ments. Therefore, in those cases, more than one sensor is typically required to isolate the principal strains [9]. PVDF exhibits the least cross-sensitivity to lateral strain among typical piezoelectric materials. It is also at least six times more compliant than macro-fiber composites (MFC) and thirty times more compliant than PZT. These characteristics make it suitable for strain sensing applications in spite of its lower piezoelectric coefficients. Piezoelectric materials exhibit pyroelectricity under non-isothermal conditions. Thus, measurement of static or near static strain inputs requires compensation techniques to remove the pyroelectric component. Averaging the values of \$\varepsilon_1\$ and \$\varepsilon_2\$ over the electrode area \$A_S\$, (5) can be written in the Laplace domain s as

$$Q(s) = \frac{Y_1 d_{31} A_S (1 + a_r d_r \nu_1)}{1 - a_r \nu_1^2} [\varepsilon_1(s) + \kappa \varepsilon_2(s)]. \quad (7)$$

Finally, assuming pure bending of the host structure, the induced longitudinal strain \$\varepsilon_1\$ in a rectangular piezoelectric film can be related to its lateral strain \$\varepsilon_2\$ using the Poisson's ratio of the host material \$\nu_b\$ as \$\varepsilon_1 = -\nu_b \varepsilon_2\$. Thus, the uniaxial strain-charge sensitivity \$S_\varepsilon\$ of a rectangular piezoelectric sensor is given by

$$S_\varepsilon(s) = \frac{Q(s)}{\varepsilon_1(s)} = \frac{Y_1 d_{31} l_s w_s (1 + a_r d_r \nu_1)(1 - \kappa \nu_b)}{1 - a_r \nu_1^2}, \quad (8)$$

where \$l_s\$ and \$w_s\$ are the length and width of the rectangular gage, respectively. The above equation suggests that the strain-charge relationship of the piezoelectric sensor is independent of frequency.

3. Charge amplifiers

Charge amplifiers are transimpedance circuits with first-order high pass filter characteristics that convert the charge produced by a piezoelectric sensor into measurable voltage [22]. A basic charge amplifier can be realized using discrete electronic components designed with an operational amplifier and an \$RC\$ feedback network as shown in Fig. 2. A piezoelectric sensor can be modeled as a capacitor \$C_S\$, with a finitely large output impedance \$R_S\$ connected in parallel to a charge source \$Q_S\$. For designs meant for near static applications, we analyze the circuit in the frequency and time domains. Ideally, the operational amplifier is assumed to possess infinite open-loop gain and infinitely high input impedance. For realistic analysis, the operational amplifier will be assumed to possess large but finite input resistance \$R_A\$; thus there are bias currents \$I_{B-}\$ and \$I_{B+}\$ that flow into its inverting and non-inverting terminals, respectively.

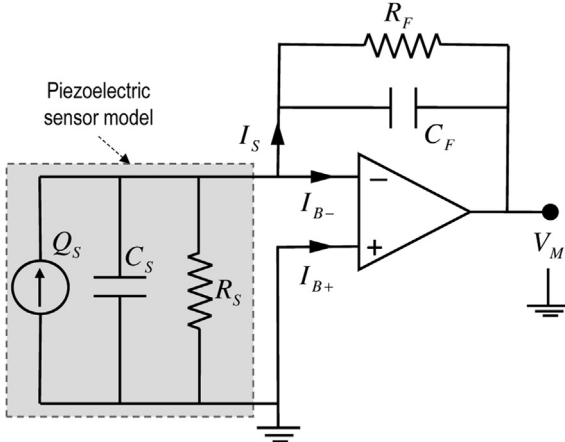


Fig. 2. Schematic of a piezoelectric sensor connected to a basic charge amplifier with feedback capacitance C_F and resistance R_F .

3.1. Frequency domain characteristics of a basic charge amplifier

Realistically, the frequency characteristics of a basic charge amplifier are those of a band-pass filter with its lower cutoff frequency determined by the sensor impedance Z_S and the feedback impedance Z_F . The upper cutoff frequency is determined by the low pass transfer function $A(s)$ of the operational amplifier [28]. The parasitic impedance contributed by leads and the operational amplifier is absorbed into the model Z_S . Therefore, the voltage per charge transfer function of a basic charge amplifier is given by

$$H_Q(s) = \frac{V_M(s)}{Q(s)} = -\frac{sA(s)Z_S Z_F}{Z_S \{A(s) + 1\} + Z_F}, \quad (9)$$

where

$$Z_S(s) = \frac{R_S}{sR_S C_S + 1}, \quad Z_F(s) = \frac{R_F}{sR_F C_F + 1}, \quad (10)$$

and R_F and C_F are the feedback resistance and capacitance, respectively. The transfer function of the operational amplifier $A(s)$ is described as a first-order transfer function

$$A(s) = \frac{A_{OL}}{s\tau_A + 1}, \quad (11)$$

where A_{OL} is the DC open-loop voltage gain and τ_A is the time constant of the operational amplifier. We define the resistance ratio $\gamma_R = R_S/R_F$ and the capacitance ratio $\gamma_C = C_S/C_F$. Therefore, using (10) and (11) in (9), one obtains the magnitude of the transfer function of the charge amplifier as

$$|H_Q(s)| = \frac{\left(\frac{A_{OL}}{C_F}\right)s}{\tau_0(1 + \gamma_C)s^2 + \left\{1 + A_{OL} + \gamma_C + \frac{\tau_A}{R_F C_F} \left(1 + \frac{1}{\gamma_R}\right)\right\} s + \frac{1}{R_F C_F} \left(1 + A_{OL} + \frac{1}{\gamma_R}\right)}. \quad (12)$$

Since $\tau_A \ll R_F C_F$, the magnitude of the transfer function of the charge amplifier at lower frequencies is reduced to a first order equation

$$|H_Q(s)| = \frac{\left(\frac{A_{OL}}{C_F}\right)s}{\left\{1 + A_{OL} + \gamma_C + \frac{\tau_A}{R_F C_F} \left(1 + \frac{1}{\gamma_R}\right)\right\} s + \frac{1}{R_F C_F} \left(1 + A_{OL} + \frac{1}{\gamma_R}\right)}. \quad (13)$$

The lower cutoff frequency f_{LC} of the above system is

$$f_{LC} = \frac{1}{R_F C_F} \left\{ \frac{1 + A_{OL} + \frac{1}{\gamma_R}}{1 + A_{OL} + \gamma_C + \frac{\tau_A}{R_F C_F} \left(1 + \frac{1}{\gamma_R}\right)} \right\} \quad (14)$$

and the passband gain or calibration factor S_Q is

$$S_Q = \frac{1}{C_F} \left\{ \frac{A_{OL}}{1 + A_{OL} + \gamma_C + \frac{\tau_A}{R_F C_F} \left(1 + \frac{1}{\gamma_R}\right)} \right\} = \frac{1 - \alpha_Q}{C_F}, \quad (15)$$

where

$$\alpha_Q = \frac{S_{Q,ideal} - S_Q}{S_{Q,ideal}}$$

is the reduction in the passband gain relative to ideal gain $S_{Q,ideal} = 1/C_F$. For ideal operational amplifiers, i.e., $A_{OL} \rightarrow \infty$, the lower cutoff frequency and the passband gain reduce to $f_{LC} = 1/R_F C_F$ and $S_Q = 1/C_F$, respectively, and thus become independent of sensor parameters. However, the effects of sensor parameters on f_{LC} and S_Q are not negligible for an operational amplifier with finite open loop gain. The lower cutoff frequency and the circuit gain are related since increasing the gain reduces the time constant of the system.

To illustrate the effect of sensor impedance on the passband sensitivity of the basic charge amplifier, we assume a typical discrete implementation of a large time constant charge amplifier with $A_{OL} = 80$ dB, $\tau_A = 1.6$ ms, and $C_F = 100$ nF and further let piezoelectric capacitance and resistance be $C_S = 1$ nF and $R_S = 1$ GΩ, respectively. Fig. 3(a) shows that for constant $R_F = 1$ TΩ and $\gamma_R = 0.001$, there is a greater reduction in gain $\Delta\alpha_Q$ for higher capacitance ratios γ_C and lower open loop gains A_{OL} . For low capacitance ratio γ_C , the calibration factor remains unaffected by parasitic capacitances, such as wire leads. Therefore, an inverting charge amplifier configuration is advantageous over a non-inverting voltage follower configuration. Fig. 3(b) shows that for constant $C_F = 100$ nF and $\gamma_C = 0.01$, the resistance ratio γ_R should be greater than at least 0.01 in order to achieve a targeted time constant of 10^5 s. This criterion for input resistance is generally met by most piezoelectric sensors for low frequency operations at room temperature.

3.2. Time domain characteristics of a basic charge amplifier

The main drawback of a large time constant charge amplifier is its sensitivity to input bias current that results in a drifting output voltage. The input bias currents I_{B-} and I_{B+} primarily originate at the supply voltage and flow into the corresponding terminals of the operational amplifier. Therefore, almost all applications involving charge amplifiers employ a finite feedback resistance on the order of $M\Omega$ to provide a DC path for the input bias current, thereby simultaneously reducing the overall time constant of the system [7,6,29]. The input bias current for commercial operational amplifiers ranges from several nA to fA. The input bias currents also exhibit a direct relationship with temperature. Hence, the net charge that is accumulated in the feedback capacitor is not only the charge generated by the piezoelectric sensor, but also the charge due to the input bias current. Using (13), the voltage response $V_M(t)$ to an ideal step charge input $Q(t)$ is thus given by

$$V_M(t) = S_Q(Q(t) + I_{B-}t)e^{-t/\tau} = S_Q Q(t)e^{-t/\tau} + e_d, \quad (16)$$

where $\tau = 1/2\pi f_{LC}$ is the time constant of the system and $e_d = S_Q I_{B-} t e^{-t/\tau}$ is the voltage drift rate.

Fig. 4 illustrates the effect of input bias current I_{B-} when the system is subjected to an ideal step charge input $Q(t) = 1$ nC for constant $C_F = 100$ nF and different R_F values. For a charge amplifier with a small time constant, the effect of I_{B-} is negligible. However, as the time constant is increased, the accumulated error over time could be much larger than the calibrated sensor resolution. This inhibits direct measurement readout using a charge amplifier for static measurements. The drifting output voltage also limits the operational time of the charge amplifier due to saturation. Therefore, the

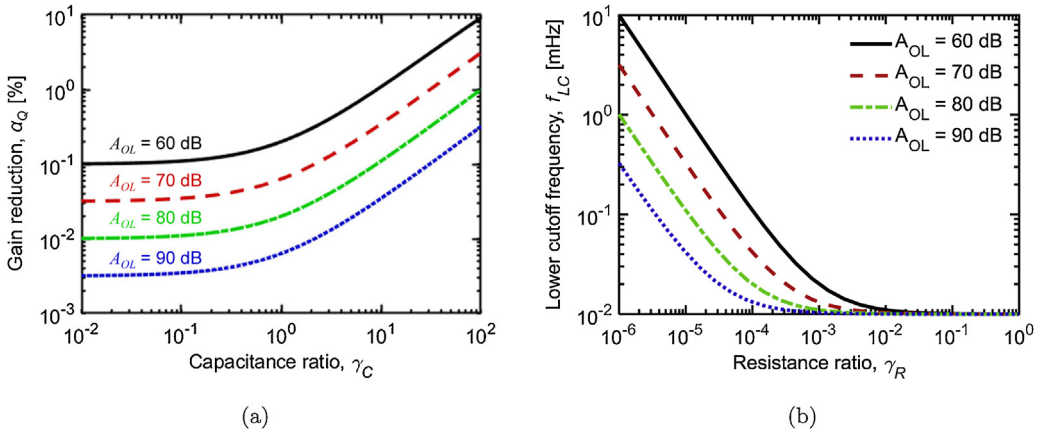


Fig. 3. (a) Effect of capacitance ratio γ_C on passband gain S_Q , (b) effect of resistance ratio γ_R on lower cutoff frequency f_{LC} for different DC open loop gains A_{OL} of the operational amplifier.

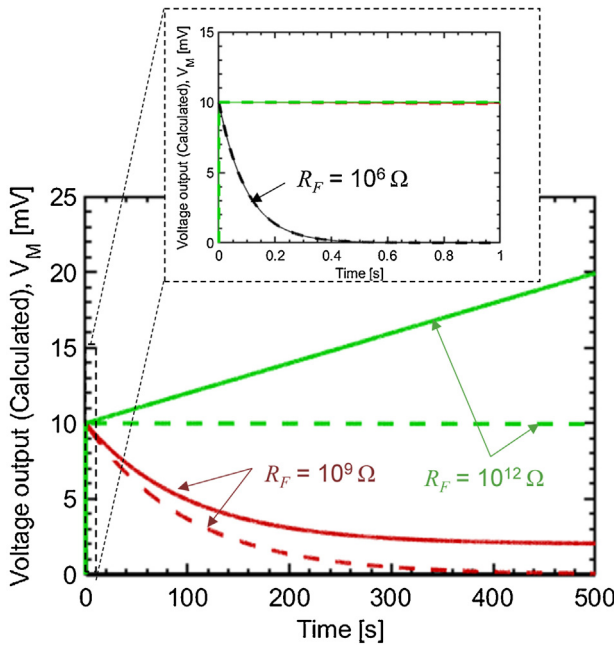


Fig. 4. Time response of a basic charge amplifier subject to an ideal step input having an operational amplifier with $I_{B-} = 2$ pA (solid lines) and $I_{B-} = 0$ (dashed lines) for different feedback resistances, R_F .

time taken for the output voltage to saturate with no charge input is given as

$$t_{sat} = \frac{V_S}{S_Q I_{B-}}, \quad (17)$$

where V_S is the upper rail voltage. For a given charge sensitivity, the operational time of the charge amplifier can be increased by using a low input bias current operational amplifier (< 2 pA) at a higher supply rail voltage. In addition to voltage drift due to input bias currents, an operational amplifier can also have a constant offset voltage. However, for long time static measurements, the influence of offset voltage is typically an order of magnitude lower than the voltage drift. In general, the offset voltage can also be reduced by utilizing an operational amplifier with a high common-mode rejection ratio [22].

Finally, Fig. 5(a) shows the inverse relationship between S_Q and τ for $R_F = 1$ TΩ and Fig. 5(b) shows the direct relationship of e_d with I_{B-} and S_Q . It is observed that a smaller S_Q is desired for maximizing τ and minimizing e_d . For example, if $I_{B-} = 2$ pA, the maximum

attainable circuit gain is 0.004 mV pC $^{-1}$ for an application requiring $\tau \geq 10^5$ s and $e_d \leq 10$ μ V s $^{-1}$. This value is very low for most practical applications and requires a higher strain sensitivity S_e . Thus, there is a need to develop an effective methodology to reduce e_d while simultaneously increasing S_Q .

4. Proposed compensated charge amplifier topology

Various techniques for automated drift compensation have been proposed in the literature [20,30,31]. Most of these solutions have been developed for specific applications and require complex implementation schemes. This article proposes a straight-forward, analog implementation of a differential charge amplifier topology that effectively compensates for drift in the output voltage and simultaneously doubles the gain of the basic charge amplifier. The underlying principle of this technique is real time drift cancellation through construction of a parallel charge amplifier of equal charge sensitivity. The second stage of this parallel configuration is the inverting amplification stage, which provides further drift compensation and also compensates for the gain reduction in the first stage due to large time constant requirements. The proposed topology provides a differential output, thereby reducing ground loop noise. Further, the output voltage always corresponds to the state of strain in the sensor, providing a direct measurement readout.

Consider the differential compensated charge amplifier topology in Fig. 6 with passband sensitivities S_{Q1} and S_{Q2} and lower cutoff frequencies f_{LC1} and f_{LC2} . The input bias currents flowing into the corresponding inverting terminals of the operational amplifiers are I_{B1-} and I_{B2-} . Generally, I_{B1-} is assumed to be equal to I_{B2-} [14,19,22] but the variation between the bias currents accumulates as error and becomes significant for long time static measurements. Let insulation resistances of the capacitors R_{F1} and R_{F2} equal 1 TΩ. The output from the first stage is fed into standard inverting amplifiers with gains given by $r_{G1} = -R_2/R_1$ and $r_{G2} = -R_4/R_3$. Using (13), the output voltage $V_M(s)$ for a step input to the compensated charge amplifier is given by

$$V_M(s) = \left(\frac{S_{Q1}r_{G1}}{s + f_{LC1}} + \frac{S_{Q2}r_{G2}}{s + f_{LC2}} \right) sQ(s) + \left(\frac{S_{Q1}r_{G1}I_{B1-}}{s + f_{LC1}} - \frac{S_{Q2}r_{G2}I_{B2-}}{s + f_{LC2}} \right). \quad (18)$$

Let the tolerances of the feedback capacitance, inverting gain, and input bias current be t_C , t_r , and t_B , respectively. Then $S_{Q2} = S_{Q1}/(1 - t_C)$, $r_{G2} = (1 - t_r)r_{G1}$, $f_{LC2} = f_{LC1}/(1 - t_C)$, and $I_{B2-} = I_{B1-}(1 - t_B)$. The effect of variations in insulation resistances of the capacitors is neglected. Therefore, the voltage/charge trans-

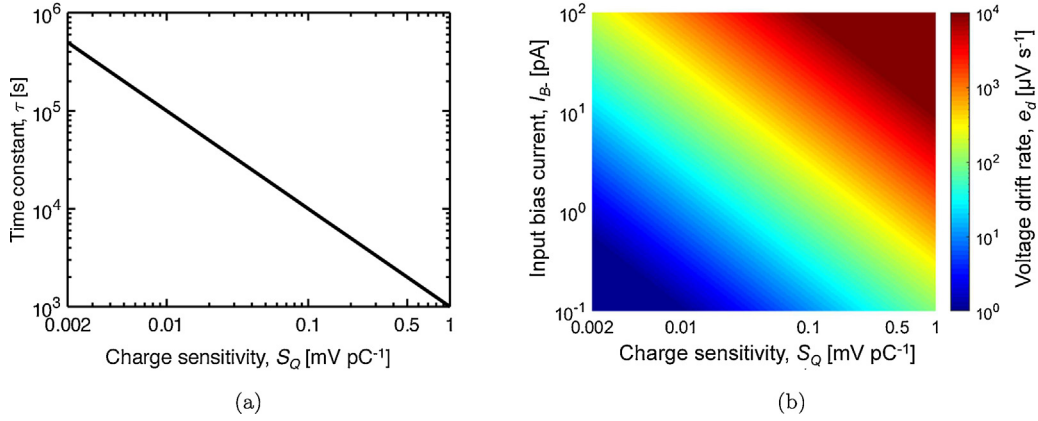


Fig. 5. (a) Time constant τ vs. charge sensitivity S_Q of a basic charge amplifier for $R_F = 1 \text{ T}\Omega$, (b) effect of charge sensitivity S_Q and input bias current I_{B^-} on voltage drift rate e_d .

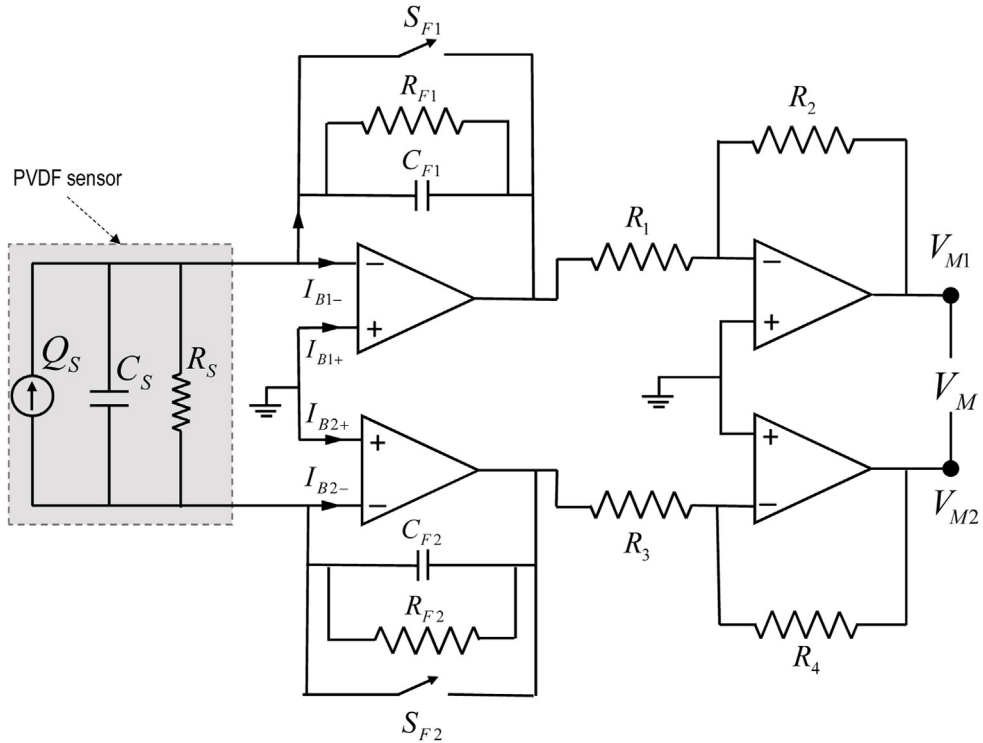


Fig. 6. Schematic of the piezoelectric sensor interfaced with the proposed differential compensated charge amplifier topology.

fer function for the compensated charge amplifier in the Laplace domain is given by

$$H_{CQ}(s) = \frac{V_M(s)}{Q(s)} = sS_{Q1}r_{G1} \left\{ \frac{s(2-t_C-t_r)+f_{LC}(1-t_r)}{s^2(1-t_C)+sf_{LC}(2-t_C)+f_{LC}^2} \right\} \quad (19)$$

and the residual drift rate in the Laplace domain is given by

$$R_{CD}(s) = S_{Q1}r_{G1}I_{B1-} \left\{ \frac{s(t_r+t_B-t_rt_B-t_C)+f_{LC}(t_r+t_B-t_rt_B)}{s^2(1-t_C)+sf_{LC}(2-t_C)+f_{LC}^2} \right\}. \quad (20)$$

For a large time constant system, i.e., $f_{LC} \rightarrow 0$, the passband gain of the compensated charge amplifier S_{CQ} and the residual drift rate δ_r are given by

$$S_{CQ} = S_{Q1}r_{G1} \left(\frac{2-t_C-t_r}{1-t_C} \right) \text{ and } \delta_r = S_{Q1}r_{G1}I_{B-} \left(\frac{t_r+t_B-t_rt_B-t_C}{1-t_C} \right). \quad (21)$$

Finally, if there is no component variation, (21) reduces to

$$S_{CQ} = 2r_{G1}S_{Q1} \text{ and } \delta_r = 0. \quad (22)$$

If the first stage is followed by a unity gain inverting amplifier, i.e., $r_{G1} = 1$, and the component tolerances become zero, the sensitivity of the compensated charge amplifier is twice that of the basic charge amplifier with no residual drift. Thus, it allows for increasing the static sensitivity of the system, only limited by time constant requirements. However, in practice, the mismatch between components yields a small residual drift in the system.

For a discretely constructed charge amplifier, the components can be commercially procured with $t_C \leq 1\%$, $t_r \leq 1\%$, and $t_B \leq 5\%$. Fig. 7 shows the effects of circuit gain S_{CQ} and input bias current I_{B-} on the residual drift rate δ_r . A reduction of 93% of the original drift error can be achieved with the proposed topology for the above component tolerance limits. It should be noted that even though the voltage drift rate has been reduced, this does not prevent the operational amplifier from saturating. However, for a given circuit

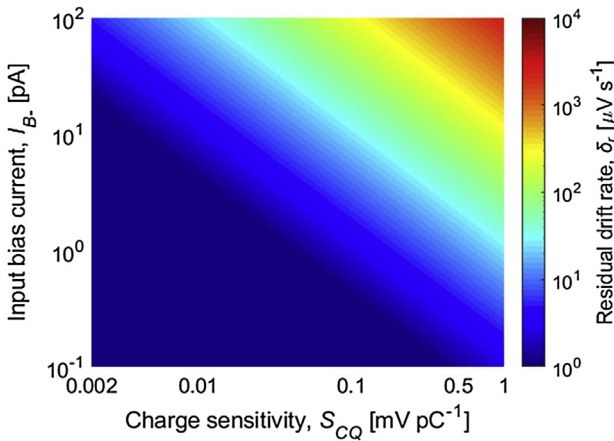


Fig. 7. Effect of S_{CQ} and I_{B-} on δ_r for $t_R = 1\%$, $t_C = 1\%$, and $t_{B-} = 5\%$.

gain, the saturation time of the proposed configuration is twice that of the basic configuration. Considering the previously stated example application requirements of $\tau \geq 10^5$ s and $e_d \leq 10 \mu\text{Vs}^{-1}$ with $I_{B-} = 2 \text{ pA}$, a static sensitivity S_{CQ} of up to 0.15 mV pC^{-1} is achieved. This is 30 dB higher than the sensitivity that can be achieved with a basic charge amplifier of the same configuration. The saturation time t_{sat} for the above configuration without an intermittent reset is 9.2 h, which is finite but sufficient for the example requirements. While there could be cases where the desired sensitivity from a signal conditioner can be achieved by modifying both feedback capacitance and inverting gain, it is always recommended to keep the inverting gain at a minimum for better noise immunity and higher frequency bandwidth [22]. Higher gain set by the second stage also tends to amplify the residual offset voltage. However, higher residual offset can be decreased by introducing a voltage bias at the non-inverting terminal of either of the charge amplifiers. The errors due to residual charges in the feedback capacitors at the start of the measurement can be eliminated by implementing reset switches S_{F1} and S_{F2} across them, which forces the output voltage to zero prior to the start of the measurement. Since no intermittent switching operation is performed during the measurement as in [18,19], error due to charge injection is also kept at a minimum. Finally, bias current tolerances can be minimized by using operational amplifiers fabricated on the same chip [19]. Hence, the proposed topology can be implemented on a quad operational amplifier that provides both compactness and minimal error. Since the input bias current increases with an increase in temperature, the residual drift also increases, warranting a tighter component tolerance or a constant temperature environment.

5. Experimental measurements (setup, results, and discussion)

An experimental investigation is conducted in order to characterize the standalone drift cancellation performance of the proposed charge amplifier and to demonstrate the suitability of PVDF as a highly sensitive active material for near static and low frequency strain measurements. A cantilever beam is chosen as a representative structure to demonstrate the performance of the PVDF strain sensor. The static performance of the strain sensor is tested through application of constant loads and the low frequency performance of the strain sensor is tested through application of sinusoidal displacement inputs with an electrodynamic shaker. Since the shaker could not produce inputs below 0.01 Hz, the low frequency performance is evaluated from 0.01 Hz to 20 Hz. It will be shown that the strain sensitivity of the sensor at dc is measured to be same as the sensitivity at 0.01 Hz. The experiments are also

used to validate the strain sensor model presented in Section 2. All measurements are carried out at room temperature set at 23 °C.

5.1. Construction and standalone performance of the proposed charge amplifier

The compensated charge amplifier shown in Fig. 6 is constructed using a quad low offset, low input bias current J-FET operational amplifier TL034CN (Texas Instruments) with a chosen feedback capacitance value $C_{F1} = 100.5 \text{ nF}$ and an inverting gain $r_{G1} = 1$. Both the capacitive and the resistive tolerances t_C and t_r were measured to be less than 1%. The open-loop voltage gain of the operational amplifier is $A_{OL} = 81.5 \text{ dB}$ and the input resistance of the operational amplifier is on the order of $\text{T}\Omega$ at room temperature [32]. Normally-open switches placed across the feedback capacitors are actuated simultaneously prior to the start of the measurement to reset the circuit by draining any stored charge. An isolated dc power supply is used to supply $V_S = \pm 5 \text{ V}$ to the operational amplifier. The feedback capacitors are chosen to be of polypropylene type for their high leakage resistance values on the order of $\text{T}\Omega$. Therefore, the static charge sensitivity of the compensated charge amplifier is calculated to be 0.02 mV pC^{-1} with a lower cutoff frequency of 0.01 mHz and an upper cutoff frequency of 310 kHz . The measurements were recorded using an analog input module (NI 9239, National Instruments) every 50 ms for a total duration of 500 s.

Fig. 8(a) demonstrates the reduction in drift error due to the compensation. Both of the measured voltages from the individual basic charge amplifiers V_{M1} and V_{M2} show a linearly increasing trend due to the input bias currents I_{B1-} and I_{B2-} , respectively. A linear fit yields voltage drift rates of $9.6 \mu\text{Vs}^{-1}$ and $9.9 \mu\text{Vs}^{-1}$, respectively, with coefficient of determination R^2 greater than 0.99 for both. The output voltage V_M exhibits a residual drift δ_r of $0.3 \mu\text{Vs}^{-1}$, which represents a 95% reduction from the original drift. The residual drift is likely due to variations between the input bias currents of the quad operational amplifier, since the feedback capacitances are chosen to be equal. Fig. 8(b) shows the input referred noise spectrum of the individual basic charge amplifiers for the proposed charge amplifier at low frequencies (5 mHz to 10 Hz). In addition to an order reduction in the $1/f$ noise near dc, an overall noise reduction of 15 dBV_{RMS} is obtained due to an increase in common mode voltage rejection. The performance of the system is thus comparable to an expensive 20 fA ultra-low bias current operational amplifier. The above compensation scheme can also be implemented with this ultra-low bias current operational amplifier to further reduce the drift error, especially for applications that require higher circuit gain or longer operational time.

5.2. Static performance of PVDF strain sensor

In order to evaluate the static measuring capability of the PVDF strain sensor interfaced with the compensated charge amplifier, a rectangular sheet of polymethyl methacrylate (Plexiglass® PMMA) with the dimensions and properties given in Table 3 is used. A screw projects from the center of the beam to facilitate application of the required force or displacement. The rectangular beam is then clamped at one of its ends using a rigid steel plate in a cantilever configuration as shown in Fig. 9. A PVDF film (LDT-028K, TE Connectivity) with the dimensions and properties given in Table 3 is then bonded at the root of the cantilever. The cantilever beam is set up on an MTS Criterion® load frame with the load applied at the screw tip. The applied load is measured using an MTS load cell (LPS 504). The electrical leads from the PVDF film are connected to the differential terminals of the compensated charge amplifier and the output voltage V_M is recorded every 50 ms for 500 s.

Substituting the values from Tables 2 and 3 in (8), the strain-charge sensitivity of the PVDF strain sensor S_e is calculated to be

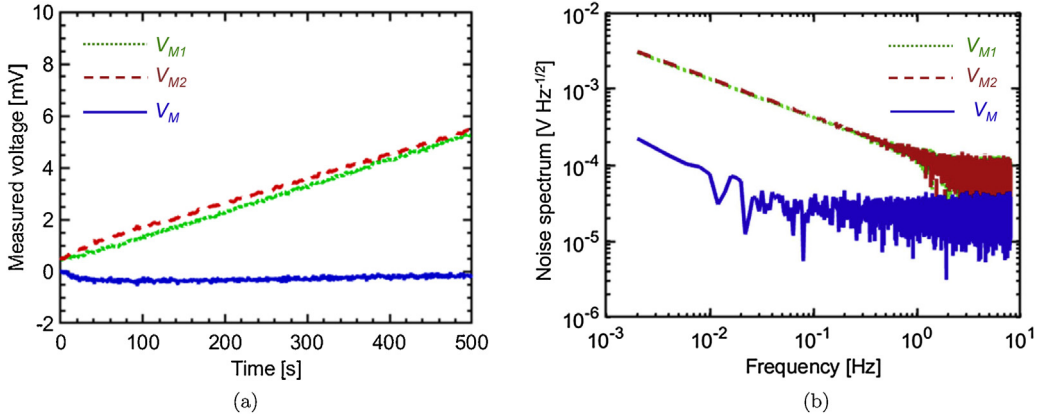


Fig. 8. (a) Measured long time performance of the compensated charge amplifier without PVDF, (b) measured noise spectrum of the compensated charge amplifier.

Table 3

Mechanical properties of the host structure and the PVDF film.

Properties of the host structure			Properties of the PVDF film		
Parameter	Units	Value	Parameter	Units	Value
Cantilever span, l_B	mm	50.84	Length, l_s	mm	30
Overall length, l_0	mm	101.68	Width, w_s	mm	12
Width, w_B	mm	42.16	Thickness, t_s	μm	28
Thickness, t_B	mm	1.7	Elastic modulus, Y_s	GPa	2
Elastic modulus, Y_B	GPa	3.3	Poisson's ratio, ν_s	No units	0.35
Poisson's ratio, ν_B	No units	0.4	Density, ρ_s	kg m ⁻³	1780
Density, ρ_B	kg m ⁻³	1180			

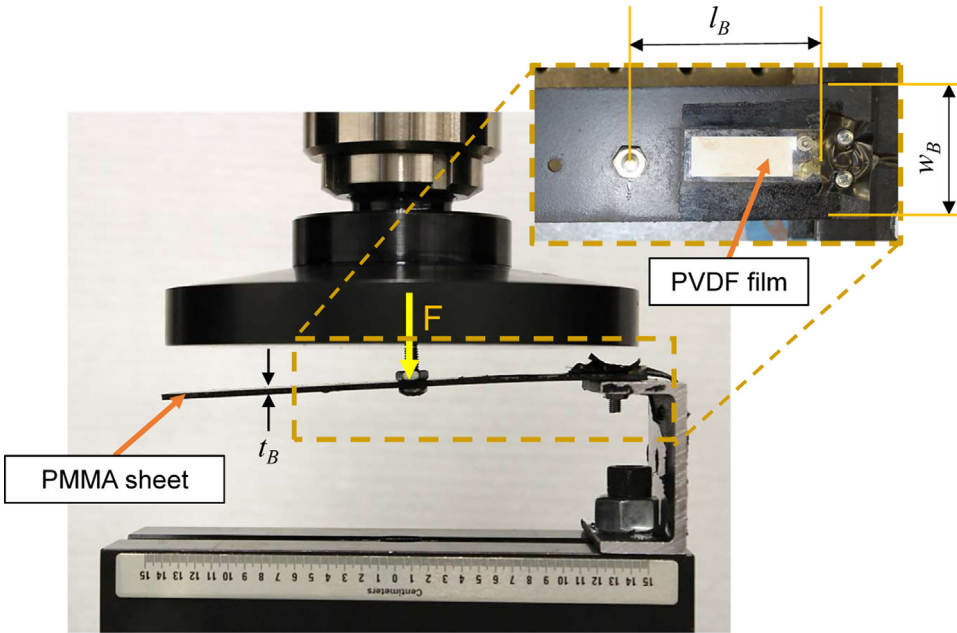


Fig. 9. Experimental setup of host structure with PVDF strain sensor on a load frame for measurement of static performance.

13.43 pC μe^{-1} . Coupling this sensor to the compensated charge amplifier of $S_{CQ} = 0.02 \text{ mV pC}^{-1}$, the overall strain sensitivity S_p is calculated to be $0.2953 \text{ mV } \mu\text{e}^{-1}$. Neglecting the inertial effect of the cantilever for low frequencies, a simplified relation between the average longitudinal strain in the PVDF film ε_1 and the applied load F is given by

$$\varepsilon_1 = \frac{6l_B}{Y_B w_B t_B^2} F. \quad (23)$$

Two sets of measurements are taken with the applied force ranging from 0.2 N to 1.4 N, which corresponds to average longitudinal strains in the cantilever from $156 \mu\text{e}$ to $1024 \mu\text{e}$. Most strain measurement applications do not exceed this range [6,33]. Since an ideal step input is not possible with the current setup, the load is ramped to the desired value using the load frame controller. The first set of measurements involves the voltages measured from the individual basic charge amplifiers with respect to ground V_{M1} and V_{M2} . Their sum would correspond to the response of the basic charge amplifier with charge sensitivity equal to that of the differ-

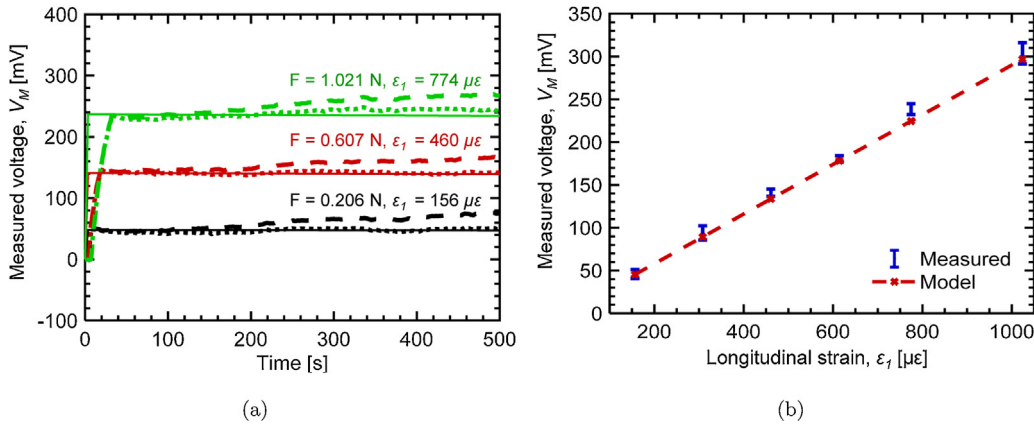


Fig. 10. (a) Measured voltages comparing the static performance of the PVDF strain sensor with the compensated charge amplifier (dotted lines), basic charge amplifier (dashed lines), and ideal step response of the strain sensor model (solid lines) with $S_{CQ} = S_Q = 0.02 \text{ mV pC}^{-1}$ at different strain levels, (b) comparison of measured voltage from compensated charge amplifier vs. model.

ential compensated charge amplifier. In this set, the output voltage is expected to drift until saturation after the application of load, since the saturation time for the operational amplifier is much lower than the time constant of the electrical circuit. As shown in Fig. 6, the second set of measurements is taken with the differential output voltage of the compensated charge amplifier V_M . Fig. 10(a) shows the static performance of the PVDF strain sensor with the proposed topology compared to the basic topology. The measured value stays within 3% of the mean voltage over the entire measurement period, thus enabling reliable near static strain measurements.

Fig. 10(b) shows the mean measured voltage with the error bars representing its variation over the holding period. The variation is bidirectional and therefore is suspected to be primarily due to the pyroelectric effect of the PVDF sensor. The pyroelectricity of PVDF is generally not significant in a typical lab environment where the rate of change in temperature is lower than the lower cutoff frequency of the material [9]. However, our sensor system (sensor and electronics) has an extremely low cutoff frequency in order to handle dc measurements, so even minor changes in temperature can affect the sensor system and become confounded with the mechanical measurement that one is trying to conduct. Other sources of error include the residual drift rate and charge leakage due to the finite impedance of the system. Using the values in Table 3 in (23) and S_p , the ideal step response of the system in the time domain is computed and found to be in good agreement with the response of the compensated charge amplifier in Fig. 10(a). Based on the static measurements, the time constant of the system is approximately 10^5 s over the measurement window, which corresponds to a lower cut-off frequency of 0.01 mHz. This range is sufficient for the purposes of this study; the methodology proposed can be used to characterize pyroelectricity and residual drift rates over longer time windows, as needed. The sensitivity of the sensor thus obtained by linear regression of the corresponding data points is $0.2937 \text{ mV } \mu\epsilon^{-1}$, which is slightly lower than the model prediction, with 5% linearity error.

5.3. Low frequency dynamic performance of PVDF strain sensor

In order to evaluate the low frequency dynamic performance (<20 Hz) of the PVDF strain sensor, a displacement input study was conducted. The setup for the experiment is shown in Fig. 11. The rectangular cantilever beam with the geometric and material properties given in Table 3 was mounted vertically as shown and the tip of the cantilever span was fastened onto the base of an electrodynamic shaker (Model ET-139, Labworks Inc.). The input displacement was kept low, so that the slope at the free end of

the cantilever can be assumed zero. The applied displacement is measured using a laser displacement sensor (Keyence LK-G32). The displacement characteristics of the electrodynamic shaker are adequate for verifying that the sensitivity is constant and phase lag is zero up to the 20 Hz limit required for our application. At low frequencies, the relationship between the longitudinal strain ϵ_1 and tip displacement x for the cantilever beam is given by

$$\epsilon_1 = \frac{1.5t_B}{l_B^2}x. \quad (24)$$

A swept sine test is performed from 0.01 Hz to 20 Hz in order to verify the performance of the strain sensor at low frequencies. The sampling frequency is chosen to be 2000 Hz. The digital swept sine is created using LabView and is converted into an analog output by an analog-to-digital signal generator (NI 9263, National Instruments) that is fed into the electrodynamic shaker. The experiment is performed at different displacement levels $x = 0.15\text{--}0.3 \text{ mm}$, corresponding to longitudinal PVDF strain levels of $172 \mu\epsilon$ to $295 \mu\epsilon$. Similar to the static performance evaluation, two sets of measurements are collected: one with the compensated charge amplifier and the other with the basic charge amplifier having the same sensitivity. Fig. 12(a) shows a representative time domain swept sine longitudinal strain input and the corresponding measured voltage at $x = 0.225 \text{ mm}$. It can be observed that for small duration of measurement, the error due to voltage drift is small (1 mV), but may become significant for longer measurements or with higher gain. It also demonstrates the ability of the sensor to measure smaller strains with the same sensitivity estimated by the static measurements. Fig. 12(b) compares the magnitude and phase of the average transfer function H_{PVDF} with the computed strain sensitivity. Since the strain sensitivity of the PVDF sensor at 0.01 Hz is measured to be the same as the sensitivity at dc, it can be assumed that there is no change in sensitivity between 0 and 0.01 Hz. The magnitude of the transfer function is found to be fairly constant up to 10 Hz, but shows higher deviation from 10 Hz to 20 Hz. The phase diagram shows that the phase difference is minimal at low frequencies but increases above 5 Hz. These deviations are due to the unmodeled dynamics of the cantilever host structure. While the cantilever structure and the shaker inputs are limited to low frequencies, the system should be able to measure strains up to the theoretical upper cutoff frequency of 310 kHz.

6. Concluding remarks

This article demonstrates a differential compensated charge amplifier for near static and low frequency strain measurements

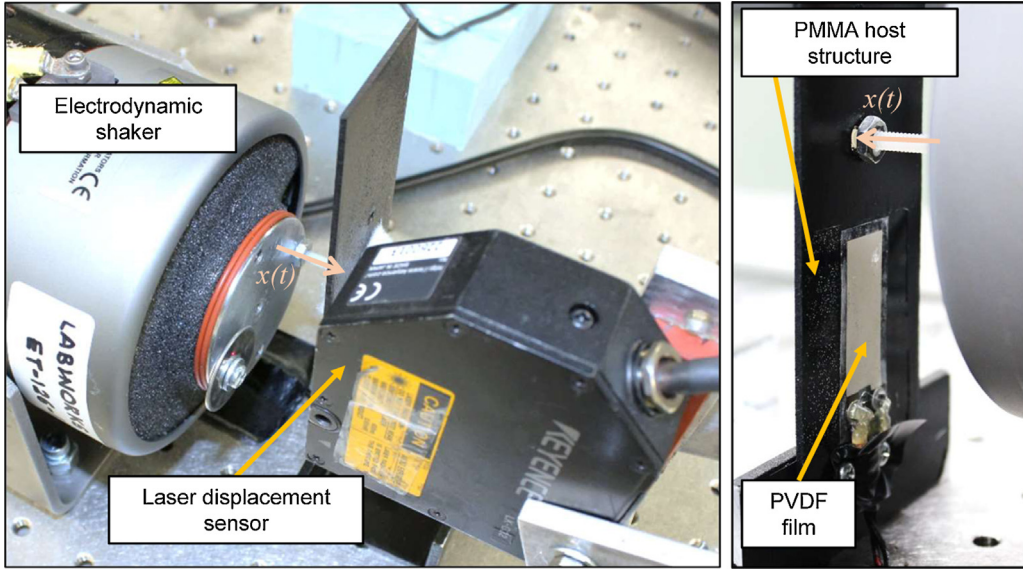


Fig. 11. Experimental setup of host structure with PVDF for low frequency dynamic measurements.

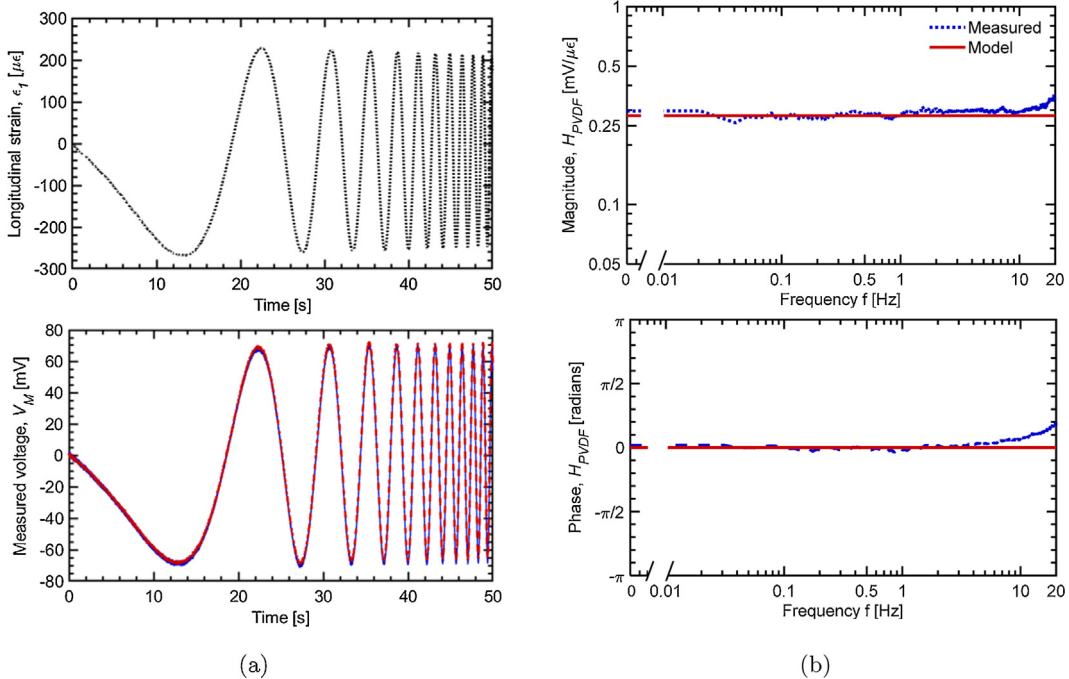


Fig. 12. (a) Measured voltages comparing the dynamic performance of the PVDF strain sensor with the compensated charge amplifier (solid blue line) and basic charge amplifier (dashed red line) in response to a low frequency swept sine strain input (dotted black line) with $S_{CQ} = S_Q = 0.02 \text{ mV pC}^{-1}$, (b) comparison of the low frequency strain-voltage transfer function H_{PVDF} measured with the compensated charge amplifier (dashed blue line) versus model (solid red line). (For interpretation of the references to color in this figure legend, the reader is referred to the web version of this article.)

with piezoelectric PVDF sensors. The conflicting requirements of maximizing the time constant of a basic charge amplifier and minimizing the voltage drift due to input bias currents are addressed through implementation of a long time constant, drift compensation circuit using commercially available components. A voltage drift reduction of up to 95% is demonstrated with a designed sensing frequency range from 0.01 mHz to 310 kHz. A theoretical sensitivity increase of up to 30 dB and overall noise reduction of 15 dBV_{RMS} is achieved with the proposed topology. The proposed circuit enables a DC voltage measurement that stays within 3% for a period of 500 s. The sensitivity computed by the strain sensor system model

agrees well with measurements with a linearity error of less than 5% up to 1 millistrain. The sensor exhibits a constant sensitivity and zero phase lag in the low frequency dynamic measurements. The variation in the output voltage during measurements is suspected to be primarily due to the pyroelectric effect of the PVDF sensor. In the future, this work will be expanded by implementing relevant temperature compensation techniques to reduce this error in strain measurements. Finally, the developed methodology can be directed towards other potential application areas, such as surface pressure, torque, and physical health monitoring applications with strain inputs in the sub-Hz frequency range.

Conflict of interest

The authors report no conflicts of interest. The authors alone are responsible for the content and writing of this article.

Acknowledgments

Financial support was provided by the member organizations of the Smart Vehicle Concepts Center, a Phase III National Science Foundation Industry-University Cooperative Research Center (www.SmartVehicleCenter.org) under grant NSF IIP 1738723.

References

- [1] H. Khan, A. Razmjou, M. Ebrahimi Warkiani, A. Kottapalli, M. Asadnia, Sensitive and flexible polymeric strain sensor for accurate human motion monitoring, *Sensors* 18 (2) (2018) 418.
- [2] L. Ma, S.N. Melkote, J.B. Morehouse, J.B. Castle, J.W. Fonda, M.A. Johnson, Thin-film PVDF sensor-based monitoring of cutting forces in peripheral end milling, *J. Dyn. Syst. Measur. Control* 134 (5) (2012) 051014.
- [3] Kulite Semiconductor Products, Kulite Strain Gage Manual, 2012.
- [4] A.S. Fiorillo, C.D. Critello, A.S. Pullano, Theory, technology and applications of piezoresistive sensors: a review, *Sens. Actuators A: Phys.* (2018).
- [5] S. Laflamme, H.S. Saleem, B.K. Vasan, R.L. Geiger, D. Chen, M.R. Kessler, K. Rajan, Soft elastomeric capacitor network for strain sensing over large surfaces, *IEEE/ASME Trans. Mech.* 18 (6) (2013) 1647–1654.
- [6] J. Sirohi, I. Chopra, Fundamental understanding of piezoelectric strain sensors, *J. Intel. Mater. Syst. Struct.* 11 (4) (2000) 246–257.
- [7] J. Rausch, C. Hatzfeld, R. Karsten, R. Kraus, J. Millitzer, R. Werthschützky, Strain measurement on stiff structures: experimental evaluation of three integrated measurement principles, *Smart Mater. Struct.* 21 (6) (2012) 064008.
- [8] I. Payo, J. Hale, Dynamic characterization of piezoelectric paint sensors under biaxial strain, *Sens. Actuators A: Phys.* 163 (1) (2010) 150–158.
- [9] L. Ma, S.N. Melkote, J.B. Morehouse, J.B. Castle, J.W. Fonda, M.A. Johnson, Design of thin-film polyvinylidene fluoride sensor rosettes for isolation of various strain components, *J. Intel. Mater. Syst. Struct.* 23 (10) (2012) 1119–1130.
- [10] L. Ngalamou, E. Ph Benech, Chamberod, Pressure measurement with resonant PVDF or copolymer, *Ferroelectrics* 171 (1) (1995) 217–224.
- [11] C.H. Lin, M.C. Tsai, S.W. Hsiao, Static force measurement for automation assembly systems, *Sens. Actuators A: Phys.* 187 (2012) 147–153.
- [12] A.V. Shirinov, W.K. Schömburg, Pressure sensor from a PVDF film, *Sens. Actuators A: Phys.* 142 (1) (2008) 48–55.
- [13] B. Thompson, H. Yoon, A prestress measurement circuit for piezoceramic stack transducers, *IEEE Sens. J.* 11 (10) (2011) 2349–2355.
- [14] I. Mahbub, S. Shamsir, S.K. Islam, S.A. Pullano, A.S. Fiorillo, A low noise front-end amplifier for pyroelectric transducer based respiration monitoring system, *IEEE 60th International Midwest Symposium on Circuits and Systems (MWSCAS)*, August 2017 (2017) 875–878.
- [15] M. Fukunaga, Y. Uesu, Compact and simple apparatus for measuring direct piezoelectricity, *Japan. J. Appl. Phys.* 42 (9S) (2003) 6115.
- [16] A. Barzegar, D. Damjanovic, N. Ledermann, P. Muralt, Piezoelectric response of thin films determined by charge integration technique: substrate bending effects, *J. Appl. Phys.* 93 (8) (2003) 4756–4760.
- [17] K.T. Park, R.D. Klafter, P.E. Bloomfield, A charge readout algorithm for piezoelectric force transducers, in: *Sixth IEEE International Symposium on Applications of Ferroelectrics*, IEEE, 1986, pp. 715–717.
- [18] D. Isarakorn, M. Linder, D. Briand, N.F. De Rooij, Evaluation of static measurement in piezoelectric cantilever sensors using a charge integration technique for chemical and biological detection, *Measur. Sci. Technol.* 21 (7) (2010) 075801.
- [19] A. Brandolini, A. Gandelli, R. Ottoboni, Silicon strategies to increase performance of piezoelectric sensors, in: *Advanced Technologies in I & M: IMTC/941994, 10th Anniversary Conference Proceedings/1994 IEEE Instrumentation and Measurement Technology Conference*, IEEE, 1994, pp. 1241–1244.
- [20] H.P. Gavin, R. Morales, K. Reilly, Drift-free integrators, *Rev. Sci. Instrum.* 69 (5) (1998) 2171–2175.
- [21] A. Ramanathan, L.M. Headings, M.J. Dapino, Near DC force measurement using PVDF sensors, in: *Smart Structures and NDE for Industry 4.0*, Vol. 10602, International Society for Optics and Photonics, 2018, pp. 106020M.
- [22] M. Massarotto, A. Carlosena, A.J. Lopez-Martin, Two-stage differential charge and transresistance amplifiers, *IEEE Trans. Instrum. Measur.* 57 (2) (2008) 309–320.
- [23] H. Zhang, S.C. Galea, W.K. Chiu, Y.C. Lam, An investigation of thin PVDF films as fluctuating-strain-measuring and damage-monitoring devices, *Smart Mater. Struct.* 2 (4) (1993) 208.
- [24] K. Kotian, L.M. Headings, M.J. Dapino, Stress averaging in PVDF sensors for in-plane sinusoidal and impact-induced stresses, *IEEE Sens. J.* 13 (11) (2013) 4444–4451.
- [25] F. Sun, A.M. Dongare, A.D. Asandei, S.P. Alpay, S. Nakhmanson, Temperature dependent structural, elastic, and polar properties of ferroelectric polyvinylidene fluoride (PVDF) and trifluoroethylene (TrFE) copolymers, *J. Mater. Chem. C* 3 (32) (2015) 8389–8396.
- [26] H. Wang, W. Cao, Determination of full set material constants of piezoceramics from phase velocities, *J. Appl. Phys.* 92 (8) (2002) 4578–4583.
- [27] S.Q. Zhang, S.Y. Zhang, M. Chen, J. Bai, J. Li, Computation of macro-fiber composite integrated thin-walled smart structures IOP Conference Series: Materials Science and Engineering, Vol. 137, IOP Publishing, 2016, pp. 012032.
- [28] P. Födisch, M. Berthel, B. Lange, T. Kirschke, W. Enghardt, P. Kaever, Charge-sensitive front-end electronics with operational amplifiers for CdZnTe detectors, *J. Instrum.* 11 (09) (2016) T09001.
- [29] C.V. Dung, E. Sasaki, Numerical simulation of output response of PVDF sensor attached on a cantilever beam subjected to impact loading, *Sensors* 16 (5) (2016) 601.
- [30] A.G. Nagornyi, A current integrator for an electrostatic accelerator energy scale calibration system, *Instrum. Exp. Tech.* 45 (1) (2002) 58–60.
- [31] K.A. Rosenbaum, S.D. Pekarek, T. Baudendistel, B. Jordan, A low-cost force sensor for electromechanical actuation systems., in: *IEEE Vehicle Power and Propulsion Conference 2007 – VPPC 2007*, IEEE, 2007, pp. 242–249.
- [32] Texas Instruments Inc, TL03x Enhanced-JFET low-power low-offset operational amplifiers, 2001.
- [33] C.C. Ma, Y.H. Huang, S.Y. Pan, Investigation of the transient behavior of a cantilever beam using PVDF sensors, *Sensors* 12 (2) (2012) 2088–2117.

Biographies

Arun Kumar Ramanathan received his B.E. degree in Automobile Engineering from Anna University, Chennai, India, in 2012 and his M.Sc. degree in Mechanical Engineering from The Ohio State University, USA, in 2017. He is currently pursuing his Ph.D. in Mechanical Engineering under the supervision of Prof. Marcelo Dapino at The Ohio State University, USA. His research interests include design, characterization, and fabrication of flexible piezoelectric sensors for vehicle applications.

Leon M. Headings is a senior research associate in the Department of Mechanical and Aerospace Engineering at The Ohio State University. He earned his Ph.D., M.S., and B.S. in mechanical engineering from The Ohio State University and his B.A. in physics from Goshen College. Prior to his graduate work, he worked in passenger and light truck tire development at Bridgestone Americas, Inc. His research interests include the modeling, characterization, development, and control of smart material devices and advanced manufacturing systems.

Marcelo J. Dapino is a professor in the Department of Mechanical and Aerospace Engineering at the Ohio State University, where he is the Honda R&D Americas Designated Chair in Engineering and Director of the Smart Vehicle Concepts Center, a National Science Foundation Industry-University Cooperative Research Center. Prof. Dapino received his Ph.D. degree from Iowa State University and his Engineering Diploma from the University of Uruguay. His research interests include smart materials and structures, advanced manufacturing, and dynamic systems.